Preferred Planar Crystal Growth and Uniform Solid Electrolyte Interface Enabled by Anion Receptor for Stable Aqueous Zn Batteries

Xinyu Wang[#1,2], Yiran Ying[#3], Xiaomin Li[#1], Shengmei Chen[4], Guowei Gao[1], Haitao Huang*[3], Longtao Ma*[2]*

[1] *Frontiers Science Center for Flexible Electronics, Institute of Flexible Electronics, Northwestern Polytechnical University, Xi'an, 710072, P. R. China*

[2] *School of Materials Science and Engineering, Guangdong Provincial Key Laboratory of Advanced Energy Storage Materials, South China University of Technology, Guangzhou 510641, P. R. China.*

[3] *Department of Applied Physics and Research Institute for Smart Energy, The Hong Kong Polytechnic University, Hung Hom, Kowloon, Hong Kong 999077, P. R. China.*

[4] *Department of Materials Science and Engineering, City University of Hong Kong, 83 Tat Chee Avenue, Kowloon, Hong Kong 999077, P. R. China.*

Corresponding authors: aphhuang@polyu.edu.hk, iamltma@nwpu.edu.cn

[#] *X. Wang, Y. Ying and X. Li contribute equally to this work.*

Experimental section

Materials

The main chemical reagents used in the experiment are: Imidazolidiny urea (ALADDIN, 98%) $NaCF_3SO_3$ (MACKLIN, 98%), $Zn(CF_3SO_3)_2$ (ALADDIN, 98%), Na_2SO_4 (SINOPHARM, AR), $ZnSO_4 \cdot 7H_2O$ (ALADDIN, AR), $NaBF_4$ (ALADDIN, AR, 99%), $Zn(BF_4)_2$ (ALADDIN, CP), $Zn(Ac)_2$ (ALADDIN, 99%), $ZnCl_2$ (Alfa Aesar, 98+%), $Zn(TFSI)_2$ (ALADDIN, 98%), Sodium bromate (MACKLIN, 99.5%), Hydrobromic acid (MACKLIN, ACS, 48%), Tetrabutylammonium bromide (ALADDIN, AR, 99%), Ketjen Black, PVDF.

The preparation and fabrication of Br_2 electrodes

In a typical synthesis, 75 mmol of $NaBrO_3$ was dissolved in 25 mL of deionized (DI) water to form solution A, 25 mL 48% HBr was added in solution A to form solution B, ultrasonic uniform dispersion. 225 mmol of $C_{16}H_{36}NBr$ was dissolved in 50 mL of deionized (DI) water to form solution C. Solution B and solution C were added to the beaker and magnetically stirred. After magnetic stirring, pour away the supernatant liquid and dry the remaining solids.

The Br_2 electrodes were prepared by a slurry coating method on carbon cloth (CFC). The Br_2 electrode is composed of 70 wt% Br_2-solids, 20 wt% Ketjen Black, and 10 wt% polyvinylidene fluoride (PVDF) binder. The electrodes were dried under vacuum at 40 °C for 12 h before cells fabrication.

Materials and electrolytes characterization

The nuclear magnetic resonance (NMR) spectra were acquired on a Bruker ADVANCE NEO 500 spectrometer using D_2O as the field frequency lock. The electrolyte structure was investigated using a Fourier transform infrared (FTIR) spectrometer (Bruker Tensor II). The Raman spectroscopy of electrolyte was tested by WITec Alpha300R. The low-temperature properties were performed in the high-low temperature test chamber. The field emission scanning electron microscope (FESEM, ZEISS, Gemini SEM 300) with an accelerating voltage of 10.0 kV was used to obtain the morphologies of Zn anode. The high-resolution transmission electron microscopy (HRTEM, Talos F200X) with an accelerating voltage of 200.0 kV was used to obtain the SEI. The Bruker D8 ADVANCED X-ray diffractometer was employed to obtain X-ray diffraction (XRD) patterns using Cu-Kα radiation (λ = 1.5418 nm).

Electrochemical measurements

The Zn||Br_2 cells were assembled in air with metallic Zn as anode, Br_2 as cathode, glass-fiber membrane (GF/A) as separator, and the prepared electrolyte. The Zn||Zn or Zn||Ti coin-type cells were assembled by a similar method. Zn||Br_2 pouch cell was also fabricated by Zn anode (10 × 10 cm), glass-fiber membrane separator (11 × 11 cm) and Br_2 cathode (10 × 10 cm) followed by packaging it with vacuum packed bag.

Electrochemical tests including LSV, CV, Tafel, EIS and IT were performed on the Correst electrochemistry workstation. LSV and CV tests were carried out on the

asymmetric Zn||Ti cells with two electrodes; EIS and IT tests were carried out on the zinc-symmetric battery with two electrodes; Tafel tests were carried out with three electrodes configuration: working electrode was Zn electrode, the counter electrode was platinum electrode, and the reference electrode was Ag/AgCl electrode. The LAND Battery Testing System was used to carry out long cycle test and multiplier test for symmetric Zn||Zn cells, long cycle test for asymmetric Zn||Cu cells and long cycle test and multiplier test for Zn||Br_2 cells.

Measurement method of ionic conductivity

Assembling Ti || electrolyte ||Ti battery tests ionic conductivity, EIS frequency range 0.01 Hz ~ 100 KHz, amplitude of 10 mV, computation formula is as follows:

$$\sigma = \frac{d}{RS} \tag{1}$$

Where σ, d, R and S represent ionic conductivity, the thickness of SPEs (0.086 cm), A. C. resistance, and the area of SPEs (1 cm^2), respectively.

Measurement method of ion migration number

Ion transfer number was calculated using the Evans-Vincent-Bruce equation:

$$t_{Zn^{2+}} = \frac{I_S(\Delta V - I_0 R_0)}{I_0(\Delta V - I_S R_S)} \tag{2}$$

Where $t_{Zn^{2+}}$ represents the ion transfer number, R_0 and I_0 are the A. C. resistance and initial current before potentiopolarization, R_s and I_s are the reaction resistance and stable current after potentiopolarization, respectively. The ΔV is the potential size. In

the test, the frequency range of EIS is 0.01Hz~100 KHz, the amplitude is 10 mV and the potentiopolarization potential is 10 mV.

Measurement method of activation energy (E_a)

Ion transfer number was calculated using the Evans-Vincent-Bruce equation:

$$R_{ct}^{-1} = Ae^{\frac{E_a}{RT}} \quad (3)$$

Where R_{ct} is the charge transfer resistance, A is the frequency factor, R is the gas constant, and T is the absolute temperature.

Computational Details

Periodic density functional theory (DFT) calculations were performed by employing the projector-augmented wave method with the VASP code.[1, 2] Perdew-Burke-Ernzerhof scheme of generalized gradient approximation[3] was used for describing the exchange-correlation functional, and DFT-D3 method[4] was used for the van der Waals interaction corrections. The kinetic energy cutoff was set as 450 eV. All the atoms in the models were allowed to relaxed, and the geometric structures were optimized until the energy and force convergence criteria of 10^{-5} eV and 0.02 eV/Å were reached. Only the gamma point was used for sampling the first Brillouin zone. A vacuum layer with a thickness of more than 20 Å was added to avoid interactions between adjacent cells.

The binding energies between molecules, anions, and Zn^{2+} were calculated by DFT in the ORCA package.[5] The structural relaxation, single-point energy calculations, and solvation free energy calculations were performed under the

B3LYP-D3BJ/6-311G*,[4, 6, 7] B2PLYP-D3BJ/def2-TZVP,[4, 6, 8] and M06-2X/6-31G* levels,[9-11] respectively. The implicit solvent model SMD was used in the calculations.[12]

Classical molecular dynamics (MD) simulations were performed by using LAMMPS code[13] with the generalized Amber force field (GAFF).[14] TIP3P model was used for water molecules,[15] and force field parameters for SO_4^{2-}, $BF4^-$, and OTf^- were taken from literature.[16-19] The initial geometric structures and parameters for the LAMMPS simulations were generated by Packmol[20] and Moltemplate[21] codes, and the numbers of molecules/anions/Zn^{2+} in the simulations were listed in **Table S1**. During the MD simulations, the time step was set as 1 fs, and energy minimization was first performed for each system with an energy tolerance of 10^{-4}. Next, each system was equilibrated for 10 ns in the NPT ensemble (Nosé–Hoover thermostat/barostat; pressure and temperature were set as 1 atm and 300 K, respectively).[22, 23] Another 5 ns simulations in the NVT ensemble (Berendsen thermostat, 300 K)[24] were subsequently performed, and the last 4 ns trajectory was used to collect the data for analysis. Periodic boundary conditions were considered in the MD simulations. Geometric structures were visualized in VESTA and VMD.[25, 26]

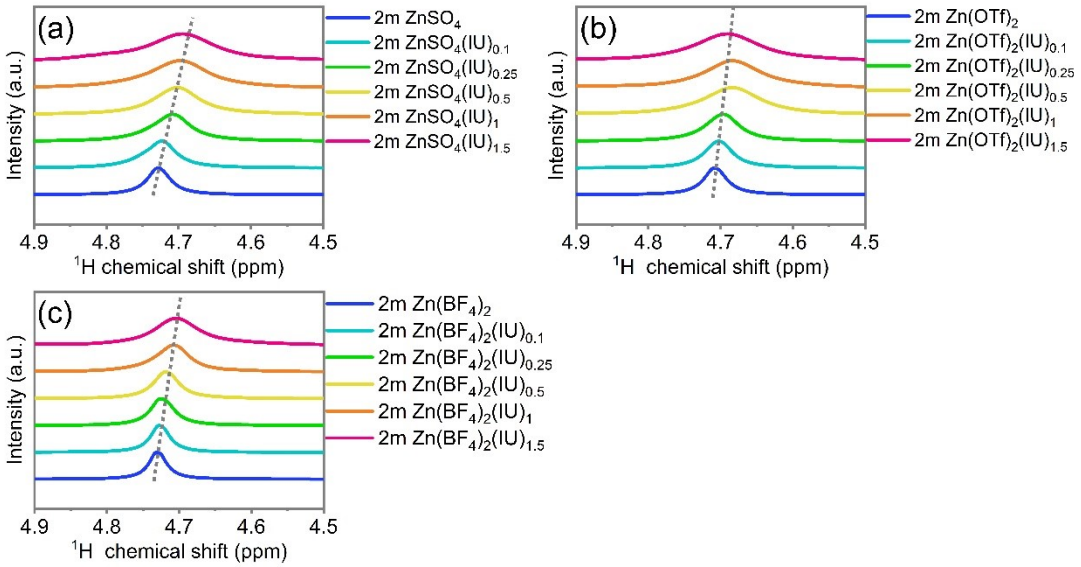

Figure S1. ^{1}H NMR spectra of (a) $ZnSO_4$, $ZnSO_4(IU)_{0.1}$, $ZnSO_4(IU)_{0.25}$, $ZnSO_4(IU)_{0.5}$, $ZnSO_4(IU)_1$, and $ZnSO_4(IU)_{1.5}$ electrolytes; (b) $Zn(OTf)_2$, $Zn(OTf)_2(IU)_{0.1}$, $Zn(OTf)_2(IU)_{0.25}$, $Zn(OTf)_2(IU)_{0.5}$, $Zn(OTf)_2(IU)_1$, and $Zn(OTf)_2(IU)_{1.5}$ electrolytes; (c) $Zn(BF_4)_2$, $Zn(BF_4)_2(IU)_{0.1}$, $Zn(BF_4)_2(IU)_{0.25}$, $Zn(BF_4)_2(IU)_{0.5}$, $Zn(BF_4)_2(IU)_1$, and $Zn(BF_4)_2(IU)_{1.5}$ electrolytes

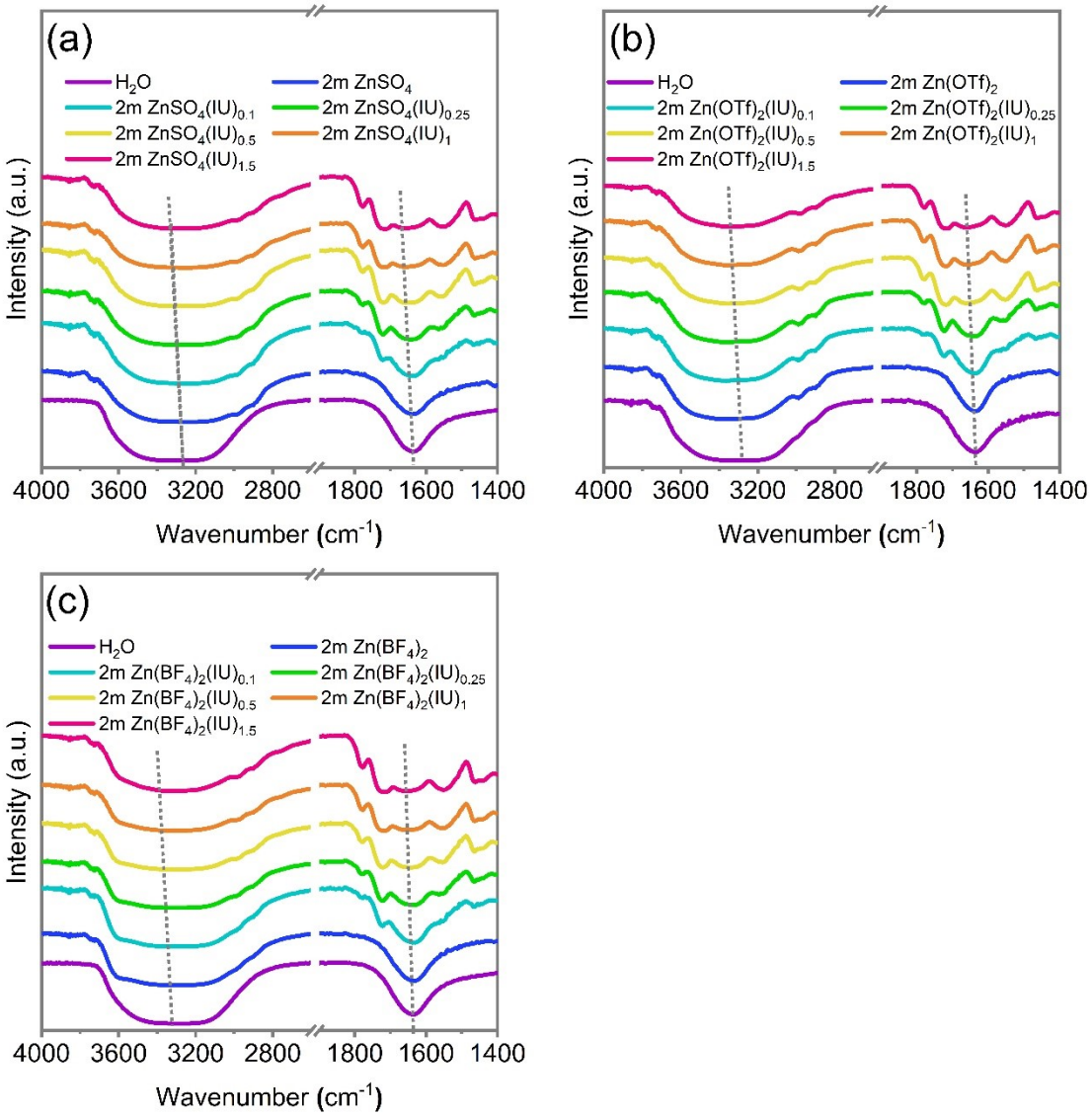

Figure S2. FT-IR spectra of (a) $ZnSO_4$, $ZnSO_4(IU)_{0.1}$, $ZnSO_4(IU)_{0.25}$, $ZnSO_4(IU)_{0.5}$, $ZnSO_4(IU)_1$, and $ZnSO_4(IU)_{1.5}$ electrolytes; (b) $Zn(OTf)_2$, $Zn(OTf)_2(IU)_{0.1}$, $Zn(OTf)_2(IU)_{0.25}$, $Zn(OTf)_2(IU)_{0.5}$, $Zn(OTf)_2(IU)_1$, and $Zn(OTf)_2(IU)_{1.5}$ electrolytes; (c) $Zn(BF_4)_2$, $Zn(BF_4)_2(IU)_{0.1}$, $Zn(BF_4)_2(IU)_{0.25}$, $Zn(BF_4)_2(IU)_{0.5}$, $Zn(BF_4)_2(IU)_1$, and $Zn(BF_4)_2(IU)_{1.5}$ electrolytes

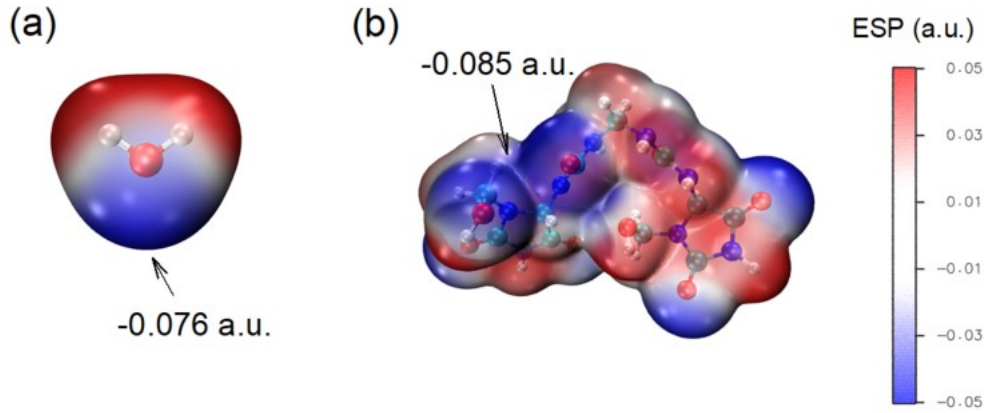

Figure S3. Electrostatic potential mapping of H_2O and IU.

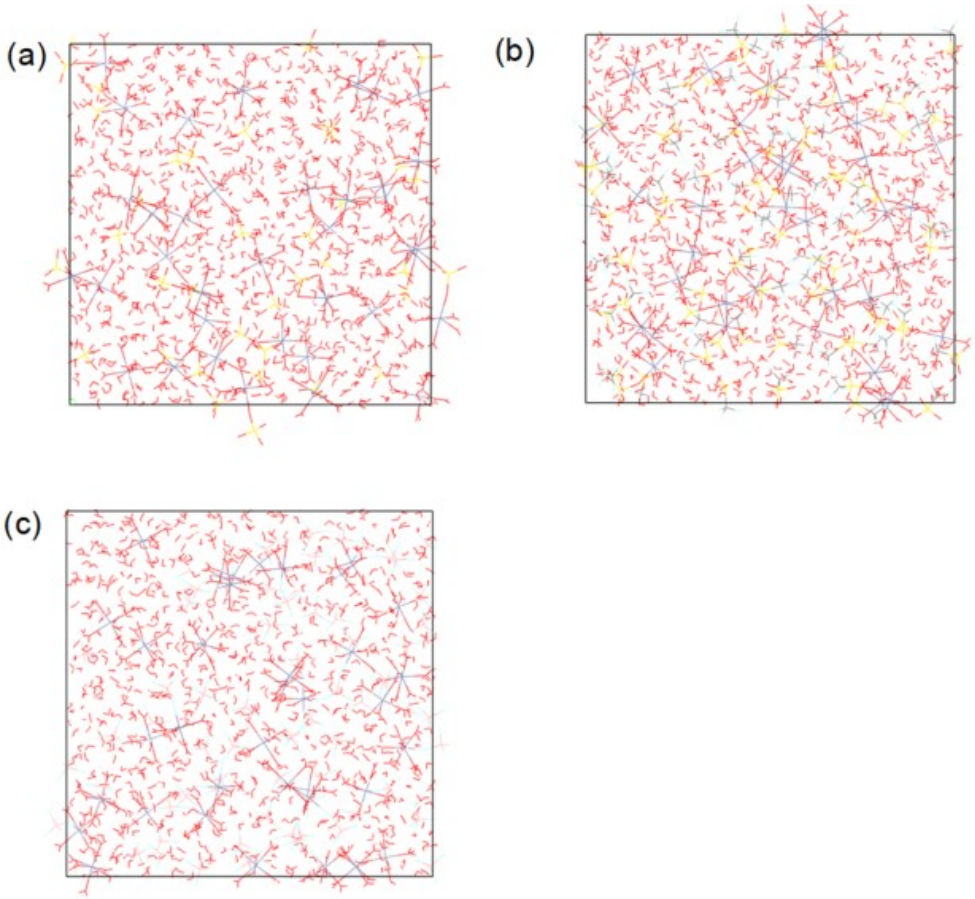

Figure S4. Snapshots during MD simulations for (a) 2m $ZnSO_4$, (b) 2m $Zn(OTf)_2$ and (c) 2m $Zn(BF_4)_2$ aqueous electrolytes. Color code for atoms: Zn, greyish blue; O, red; H, white; S, yellow; C, grey; N, blue; B, pink; F, cyan.

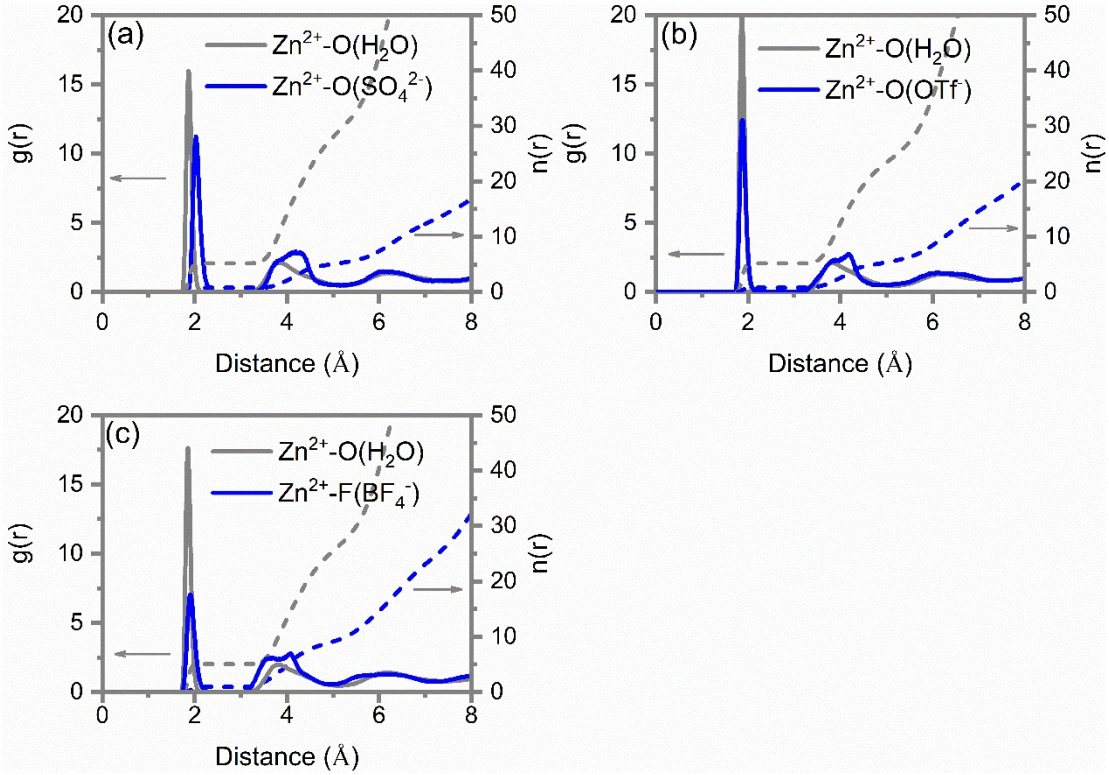

Figure S5. Zn-O/Zn-F radial distribution function (RDF) g(r) (in solid lines) and coordination number n(r) (in dashed lines) for (a) 2m $ZnSO_4$, (b) 2m $Zn(OTf)_2$ and (c) 2m $Zn(BF_4)_2$ aqueous electrolytes.

Table S1. Coordination number (CN) around Zn^{2+} of O/F atoms in H_2O, anions (SO_4^-, BF_4^-, OTf^-), and imidurea in the first solvation shell from MD simulations.

System	CN for O (H_2O)	CN for O(SO_4^-)/F(BF_4^-)/O(OTf^-)	CN for O_{CO}(IU)	CN for O_{OH}(IU)
2 M $ZnSO_4$	5.197	0.803	-	
2 M $ZnSO_4(IU)_{0.25}$	4.100	0.788	0.83	0.28
2 M $Zn(OTf)_2$	5.194	0.806	-	-
2 M $Zn(OTf)_2(IU)_{0.25}$	3.858	1.056	0.83	0
2 M $Zn(BF_4)_2$	5.055	0.945	-	-
2 M $Zn(BF_4)_2(IU)_{0.25}$	4.011	0.906	0.83	0

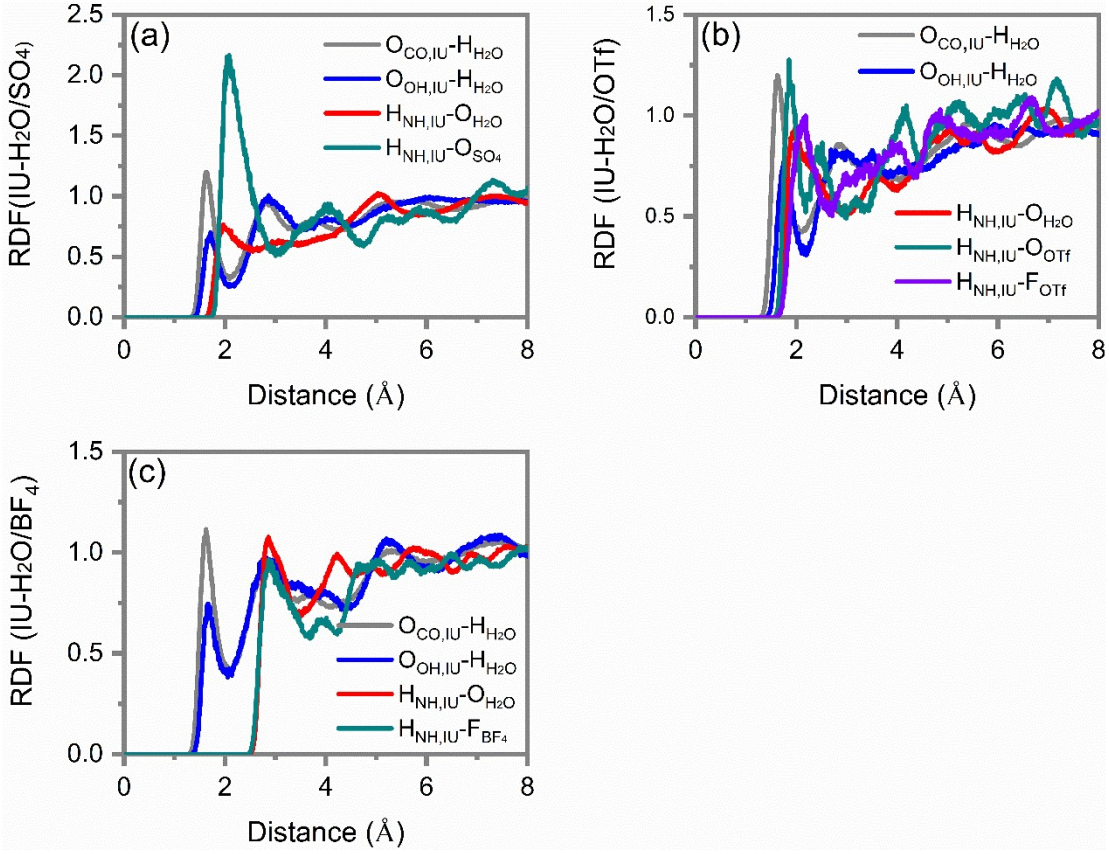

Figure S6. H-O and H-F radial distribution function (RDF) for (a) 2 m $ZnSO_4(IU)_{0.25}$, (b) 2 m $Zn(OTf)_2(IU)_{0.25}$ and (c) 2 m $Zn(BF_4)_2(IU)_{0.25}$ aqueous electrolytes. For imidurea-H_2O interactions, O_{OH}-H_{H2O}, $O_{C=O}$-H_{H2O}, and H_{NH}-O_{H2O} pairs are considered; For imidurea-SO_4^-/BF_4^-/OTf^- interactions, H_{NH}-O_{SO4}, H_{NH}-F_{BF4}, H_{NH}-O_{OTf}, and H_{NH}-F_{OTf}, pairs are considered.

Table S2. The number of molecules/anions/Zn^{2+} in electrolytes in the MD simulations.

System	Number of Zn^{2+}	Number of SO_4^-/BF_4^- /OTf^-	Number of Imidurea	Number of H_2O	Total number of atoms
2 M $ZnSO_4$	36	36	0	1000	3216
2 M $ZnSO_4(IU)_{0.25}$	36	36	9	1000	3603
2 M $Zn(BF_4)_2$	36	72	0	1000	3396
2 M $Zn(BF_4)_2(IU)_{0.25}$	36	72	9	1000	3783
2 M $Zn(OTf)_2$	36	72	0	1000	3612
2 M $Zn(OTf)_2(IU)_{0.25}$	36	72	9	1000	3999

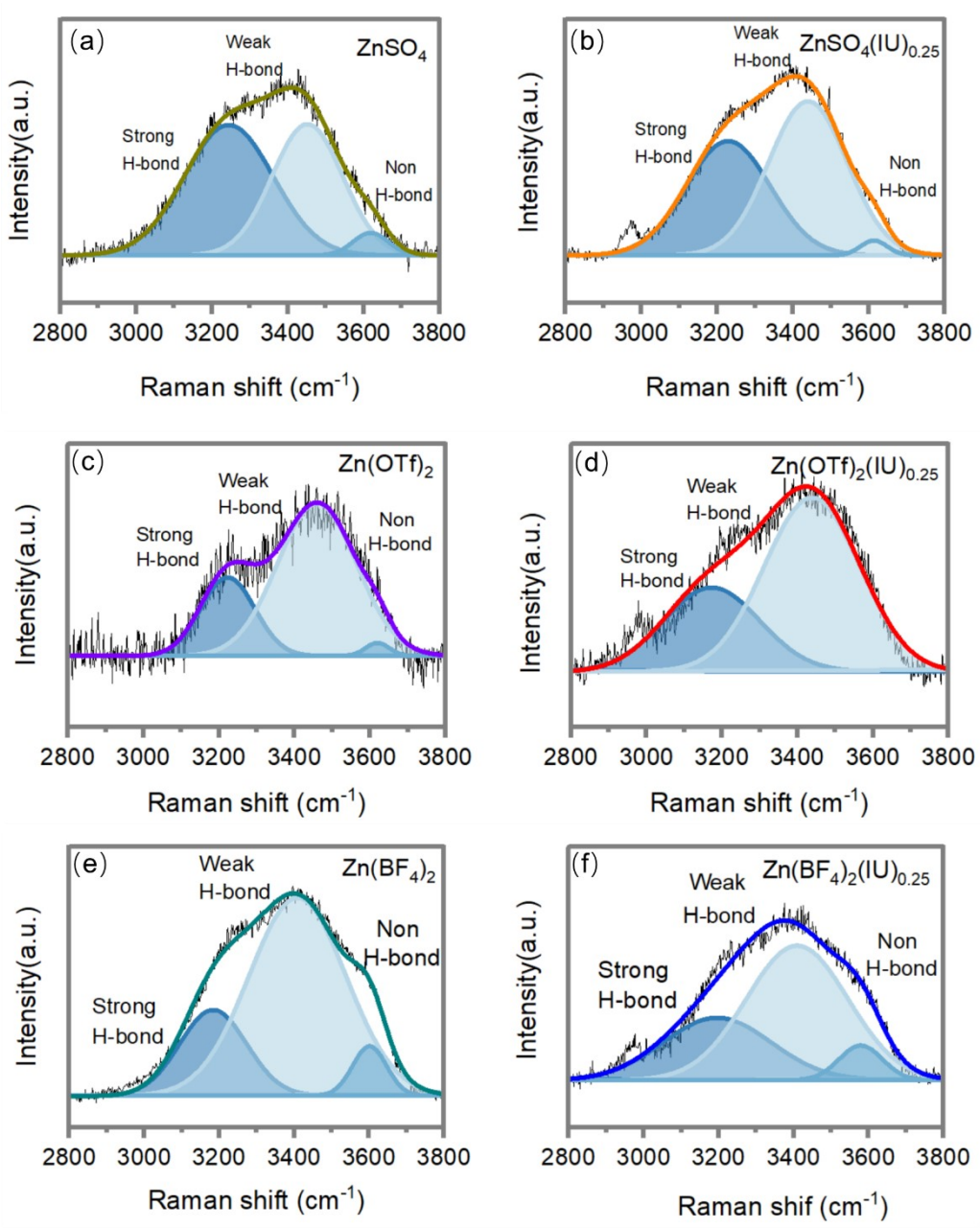

Figure S7. Raman spectra and corresponding fitted curves of -O-H stretching bond of water in (a) $ZnSO_4$, (b) $ZnSO_4(IU)_{0.25}$, (c) $Zn(OTf)_2$, (d) $Zn(OTf)_2(IU)_{0.25}$, (e) $Zn(BF_4)_2$ and (f) $Zn(BF_4)_2(IU)_{0.25}$ electrolytes. Generally, the broad peak of O-H band could be fitted as three peaks. The shoulder peak at ~3613 cm^{-1} corresponds to free O-H in water molecules (non H-bond). Peaks at ~3411 cm^{-1} and peaks at ~3254 cm^{-1} are assigned to the asymmetric O-H stretching vibration (weak H-bond) and symmetric O-H stretching vibration modes (strong H-bond), respectively.

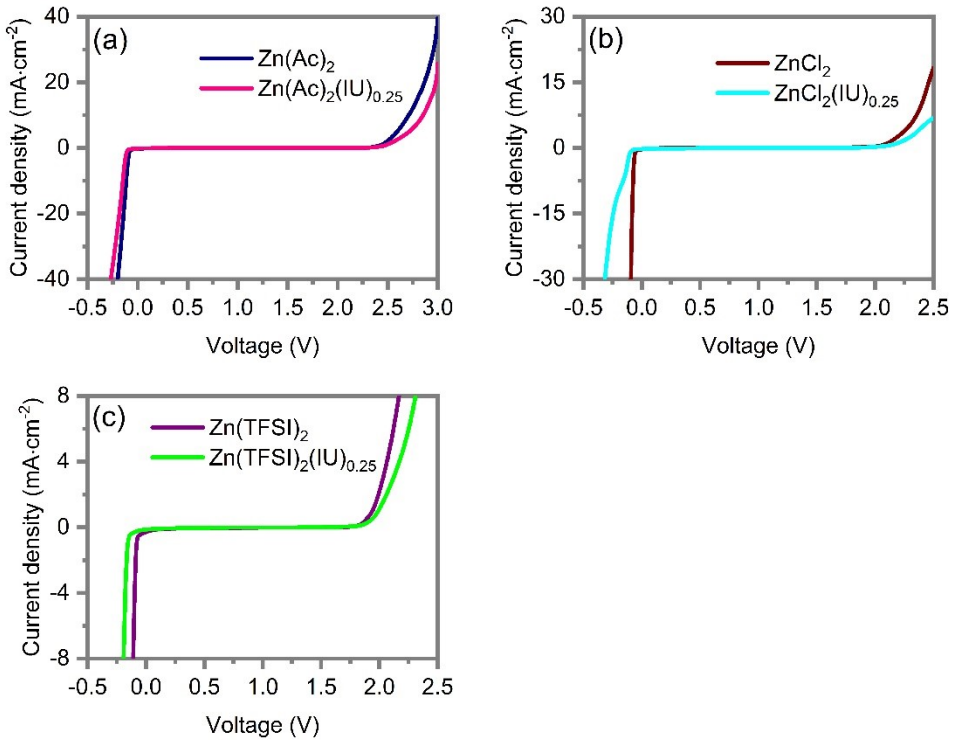

Figure S8. Electrochemical stability window of (a) $Zn(Ac)_2$, $Zn(Ac)_2(IU)_{0.25}$, (b) $ZnCl_2$, $ZnCl_2(IU)_{0.25}$, (c) $Zn(TFSI)_2$, $Zn(TFSI)_2(IU)_{0.25}$ electrolytes.

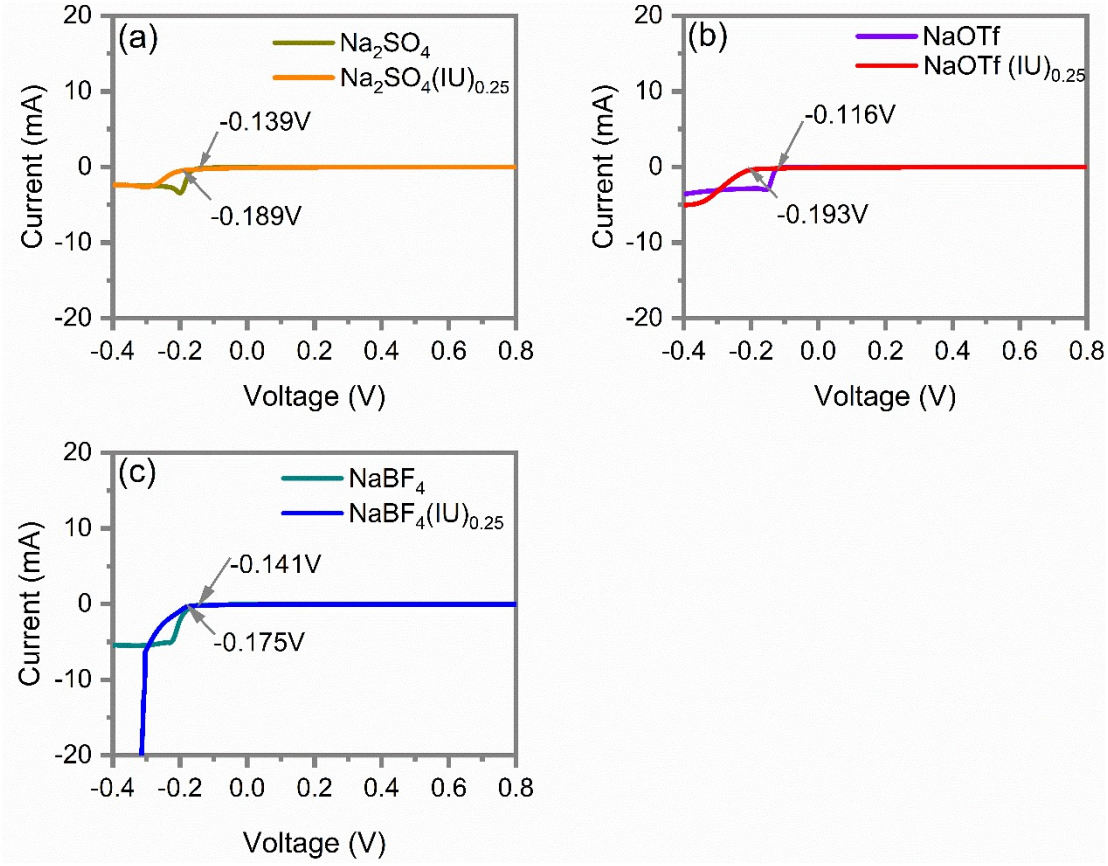

Figure S9. Linear polarization curves showing the HER on Zn metal anode using (a) Na_2SO_4, $Na_2SO_4(IU)_{0.25}$, (b) NaOTf, $NaOTf(IU)_{0.25}$ and (c) $NaBF_4$, $NaBF_4(IU)_{0.25}$ electrolytes.

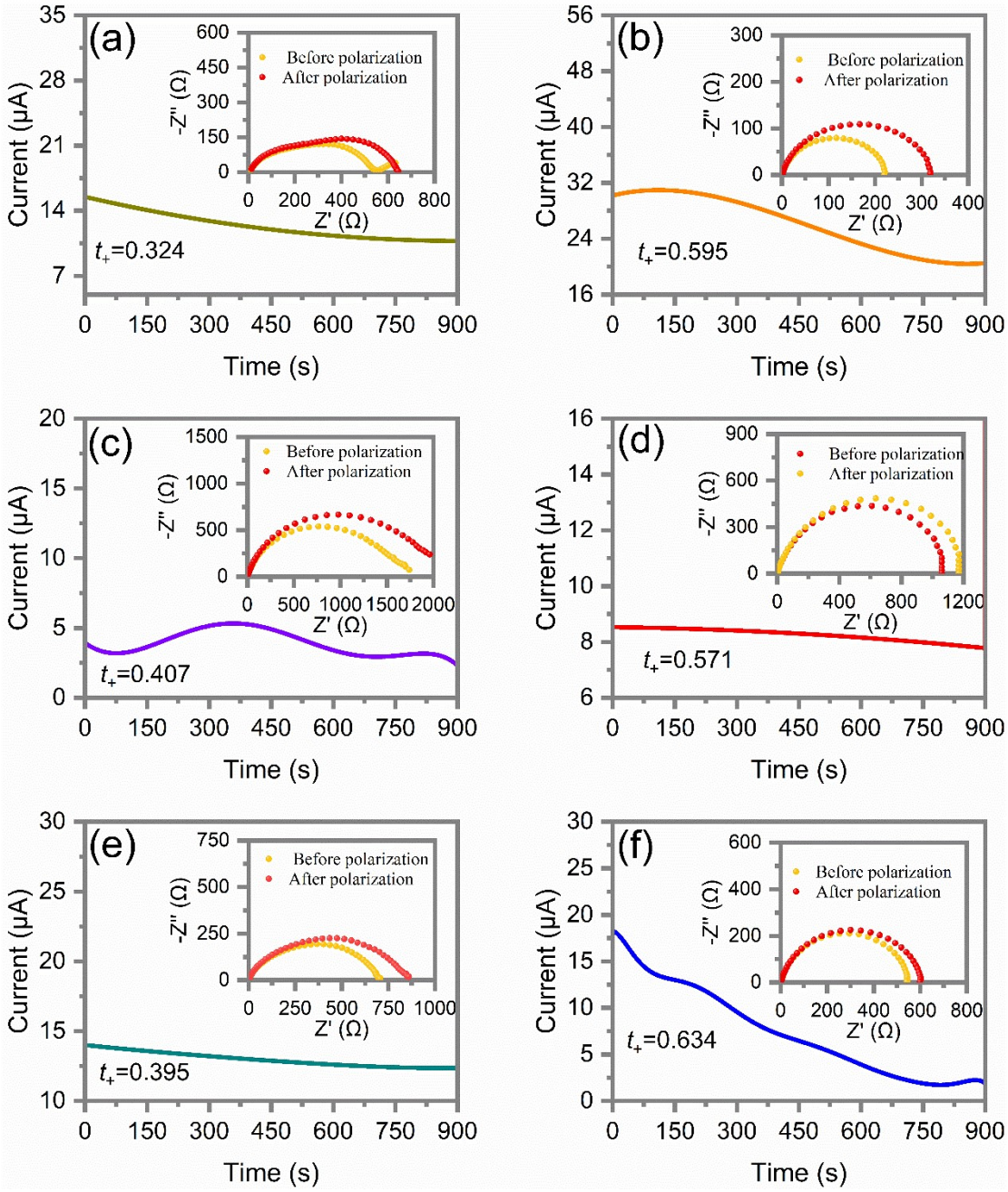

Figure S10 (a) Chronoamperograms (CAs) of Zn||Zn symmetric cells to characterize ion transfer numbers at a 10 mV overpotential using (a) $ZnSO_4$, (b) $ZnSO_4(IU)_{0.25}$, (c) $Zn(OTf)_2$, (d) $Zn(OTf)_2(IU)_{0.25}$, (e) $Zn(BF_4)_2$ and (f) $Zn(BF_4)_2(IU)_{0.25}$ electrolytes. The insets are the corresponding EIS spectra before and after polarization.

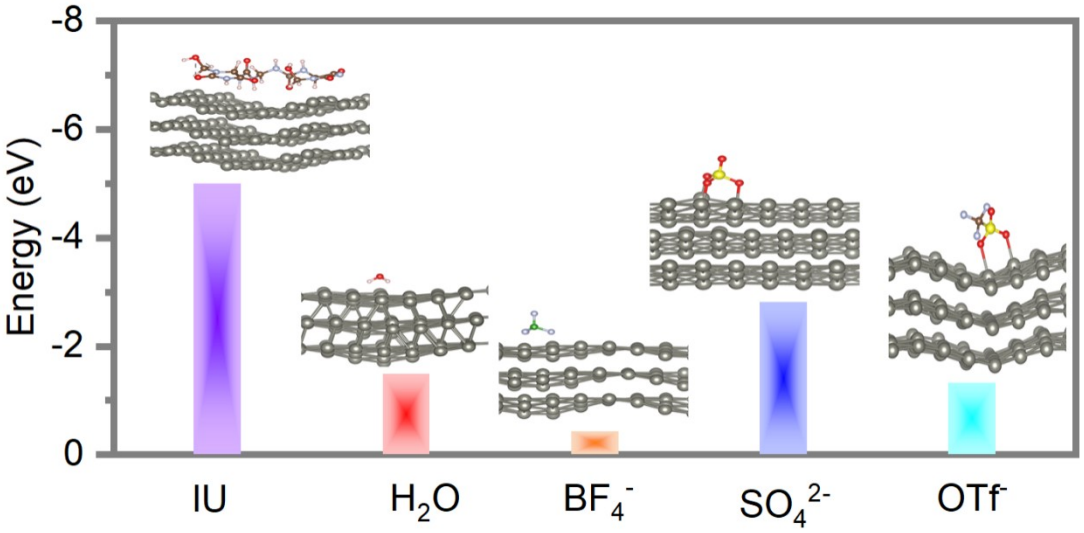

Figure S11. The adsorption energy of (a) IU, (b) H_2O, (c) SO_4^{2-}, (d) BF_4^-, and (e) OTf^- on Zn(002) surface and corresponding the most stable adsorption patterns.

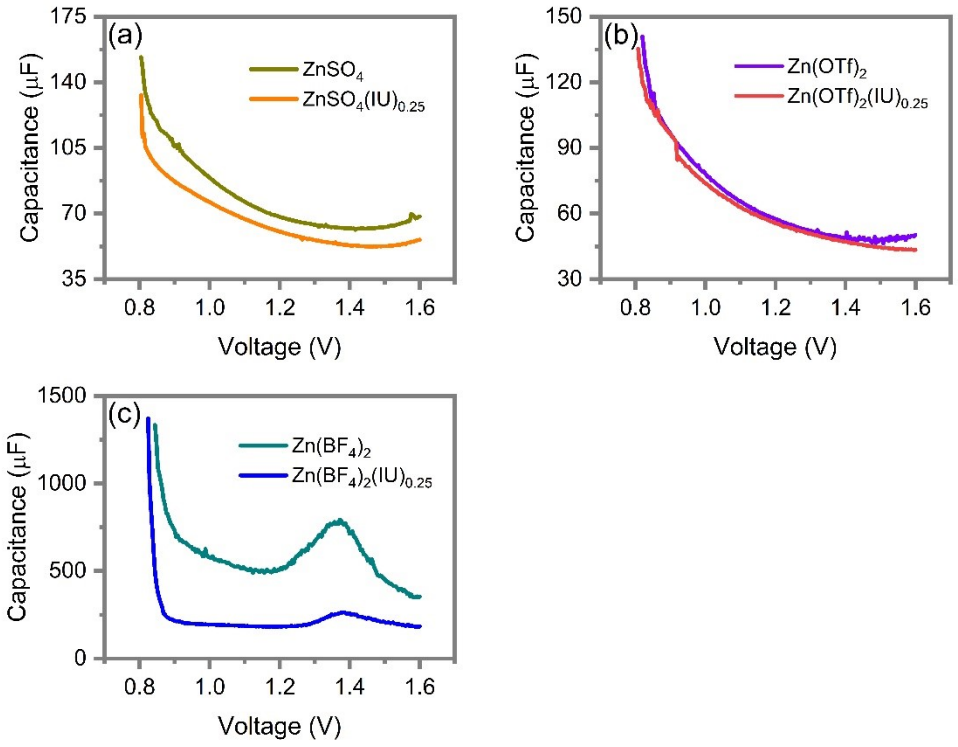

Figure S12. Differential capacitance curves for Zn in (a) 2m $ZnSO_4$, 2m $ZnSO_4(IU)_{0.25}$, (b) 2m $Zn(OTf)_2$, 2m $Zn(OTf)_2(IU)_{0.25}$, (c) 2m $Zn(BF_4)_2$, 2m $Zn(BF_4)_2(IU)_{0.25}$ aqueous electrolytes.

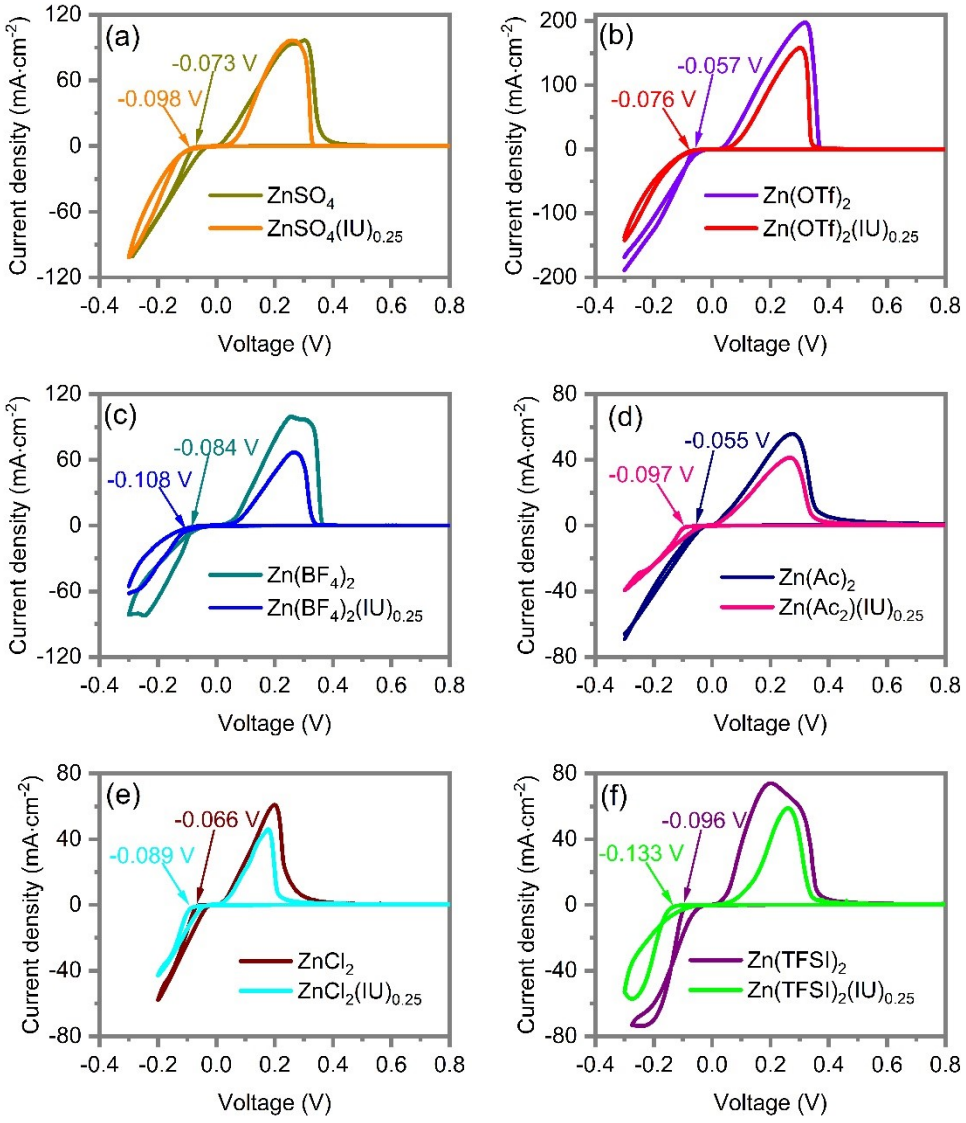

Figure S13. The CV curves of Zn||Ti asymmetric cells using (a) $ZnSO_4$ and $ZnSO_4(IU)_{0.25}$, (b) $Zn(OTf)_2$ and $Zn(OTf)_2(IU)_{0.25}$, (c) $Zn(BF_4)_2$ and $Zn(BF_4)_2(IU)_{0.25}$, (d) $Zn(Ac)_2$ and $Zn(Ac)_2(IU)_{0.25}$, (e) $ZnCl_2$ and $ZnCl_2(IU)_{0.25}$, (f) $Zn(TFSI)_2$ and $Zn(TFSI)_2(IU)_{0.25}$ electrolytes.

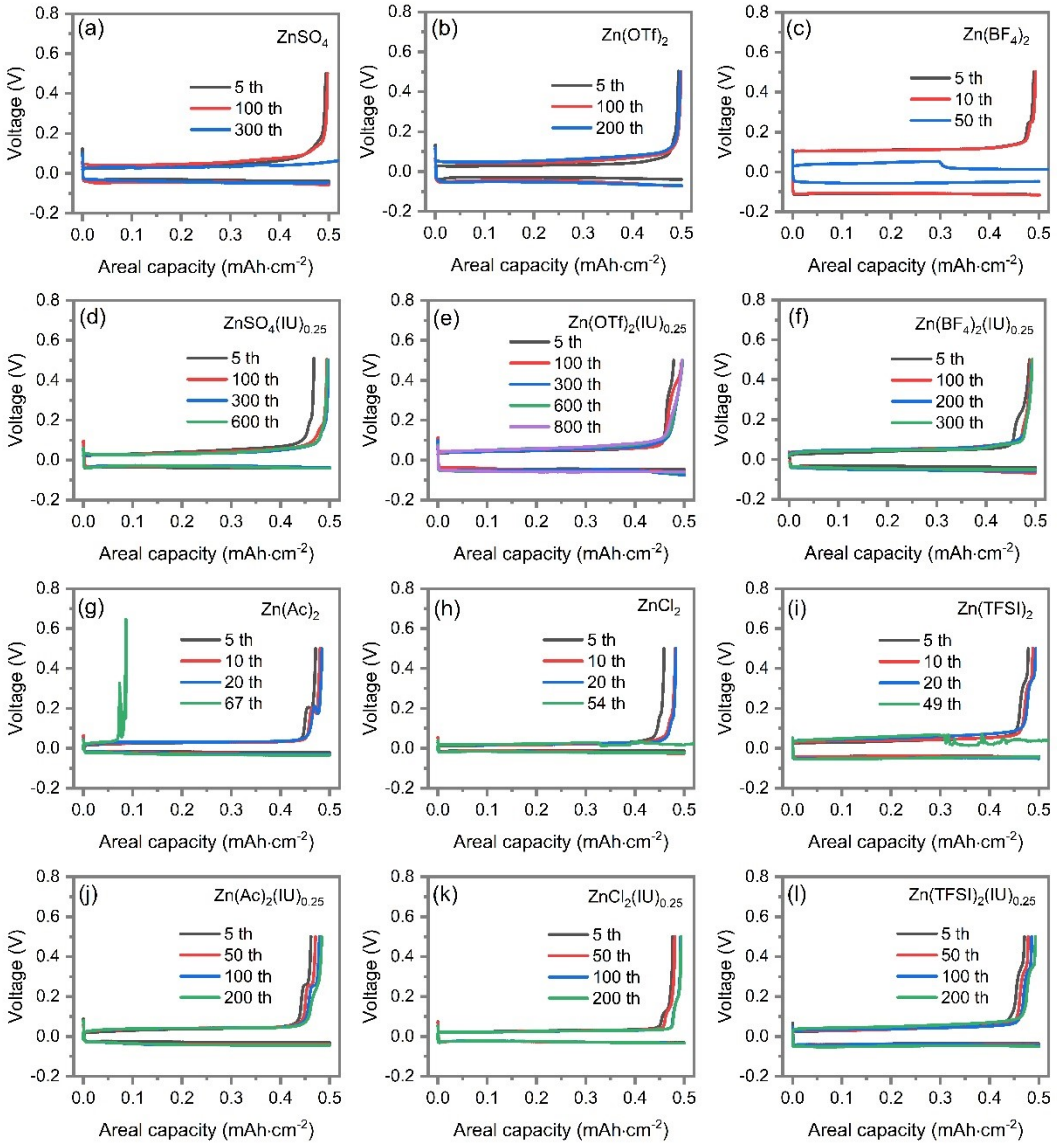

Figure S14 The charge/discharge curves of Zn||Cu asymmetric cells using (a) $ZnSO_4$, (b) $Zn(OTf)_2$, (c) $Zn(BF_4)_2$, (d) $ZnSO_4(IU)_{0.25}$, (e) $Zn(OTf)_2(IU)_{0.25}$ and (f) $Zn(BF_4)_2(IU)_{0.25}$, (g) $Zn(Ac)_2$, (h) $ZnCl_2$, (i) $Zn(TFSI)_2$, (j) $Zn(Ac)_2(IU)_{0.25}$, (k) $ZnCl_2(IU)_{0.25}$ and (l) $Zn(TFSI)_2(IU)_{0.25}$ electrolytes.

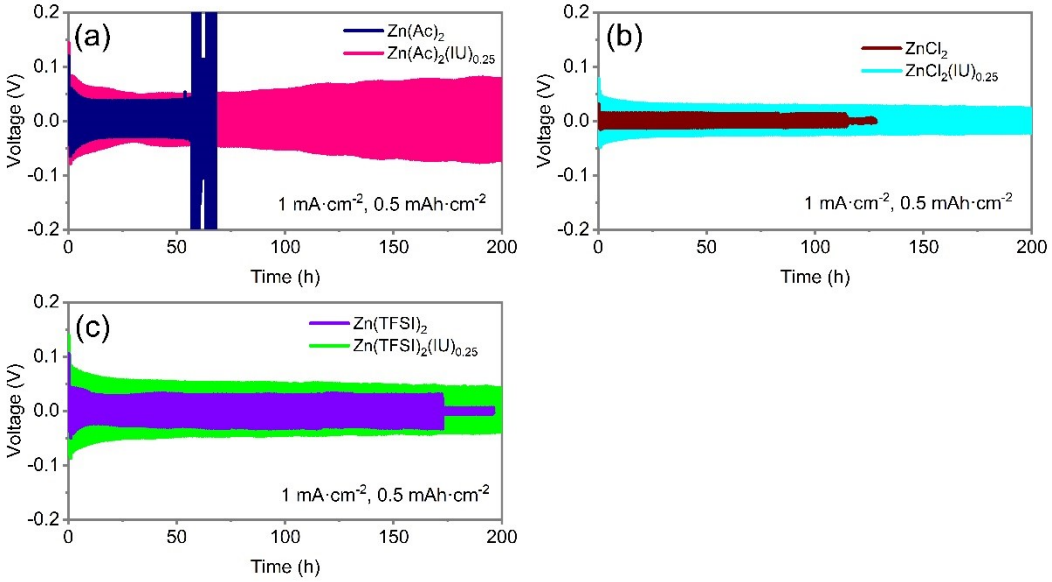

Figure S15. Galvanostatic Zn plating/stripping in Zn||Zn symmetrical cells using (a) $Zn(Ac)_2$, $Zn(Ac)_2(IU)_{0.25}$ electrolytes, (b) $ZnCl_2$, $ZnCl_2(IU)_{0.25}$ electrolytes and (c) $Zn(TFSI)_2$, $Zn(TFSI)_2(IU)_{0.25}$ electrolytes.

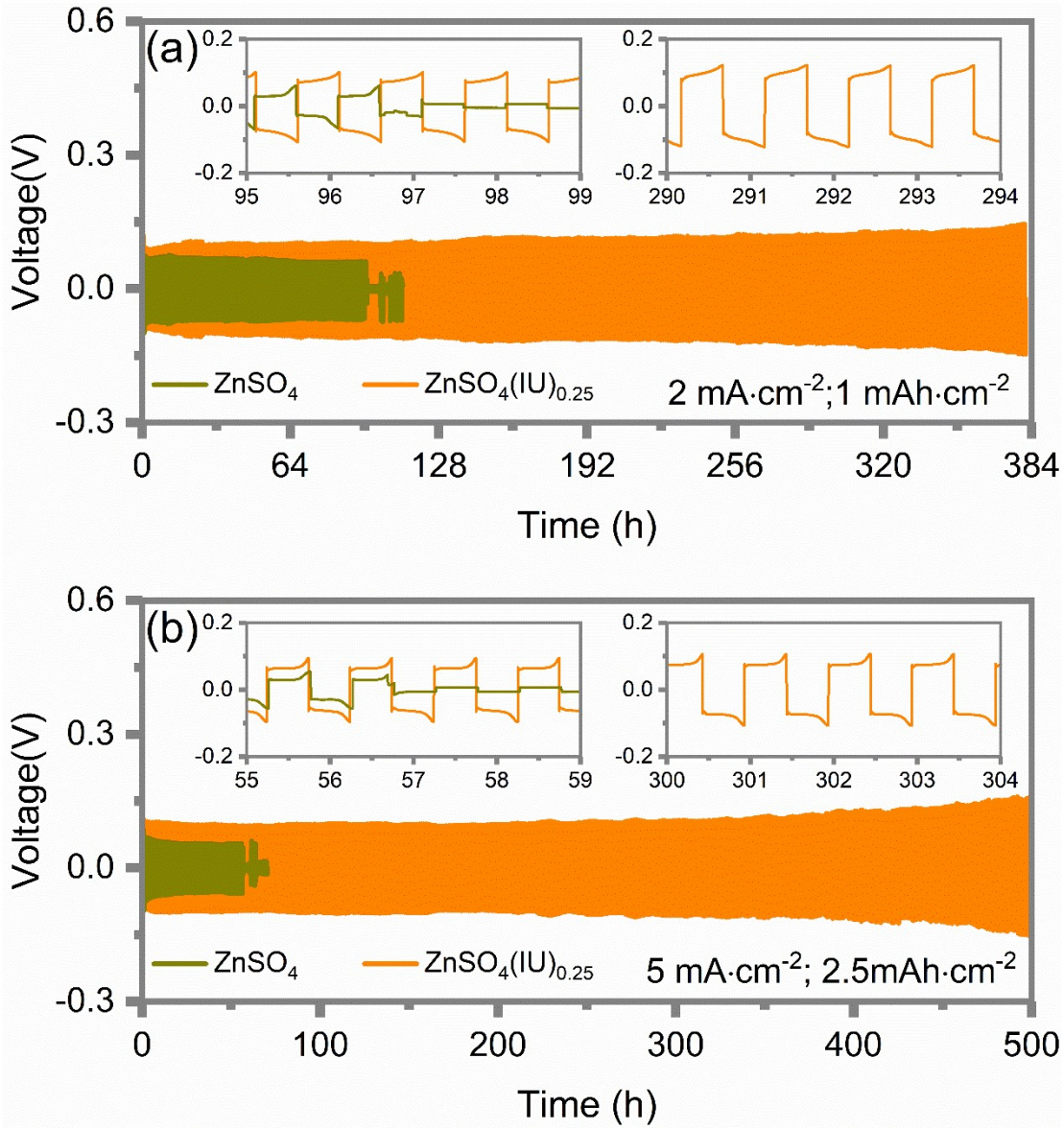

Figure S16. The charge/discharge curves of Zn||Zn symmetric cells (a) at current density of 2 mA·cm^{-2} with 1 mAh·cm^{-2} Zn cycled and (b) at current density of 5 mA·cm^{-2} with 2.5 mAh·cm^{-2} Zn cycled using $ZnSO_4$ and $ZnSO_4(IU)_{0.25}$ electrolytes.

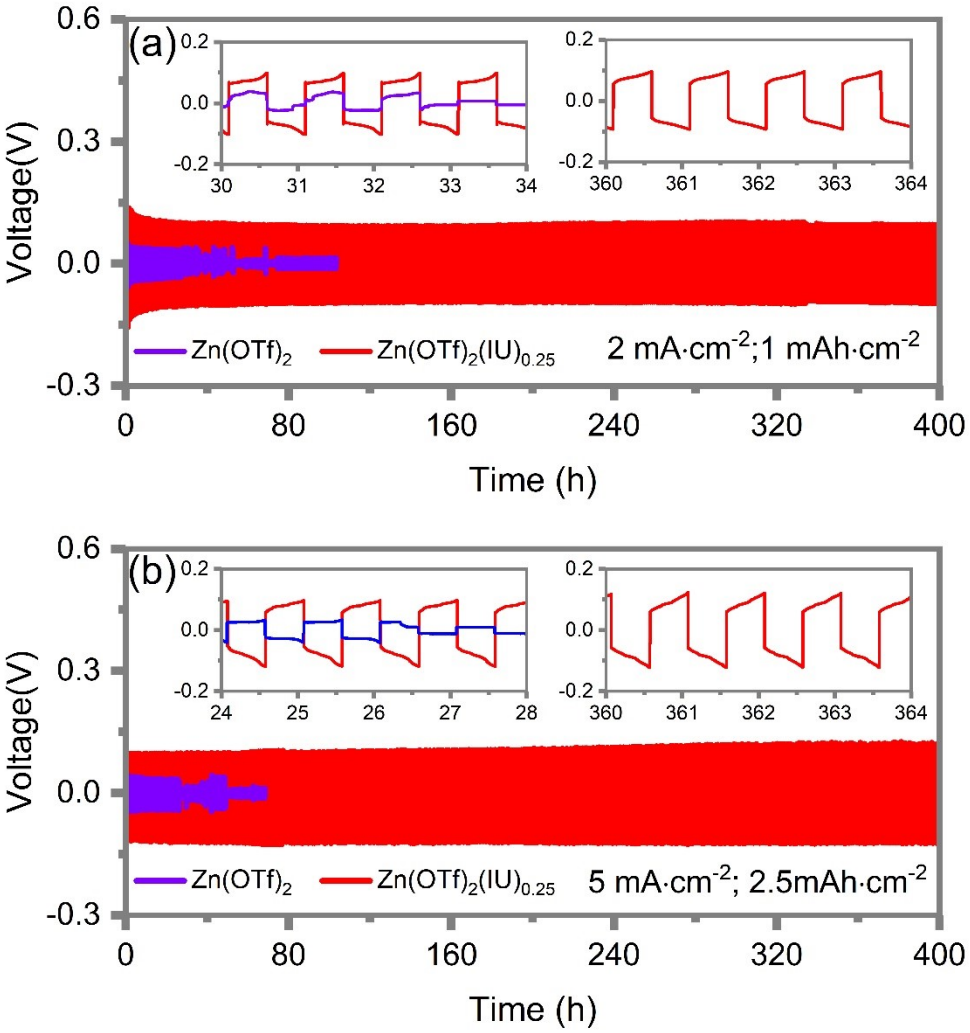

Figure S17. The charge/discharge curves of Zn||Zn symmetric cells (a) at current density of 2 mA·cm^{-2} with 1 mAh·cm^{-2} Zn cycled and (b) at current density of 5 mA·cm^{-2} with 2.5 mAh·cm^{-2} Zn cycled using $Zn(OTf)_2$ and $Zn(OTf)_2(IU)_{0.25}$ electrolytes.

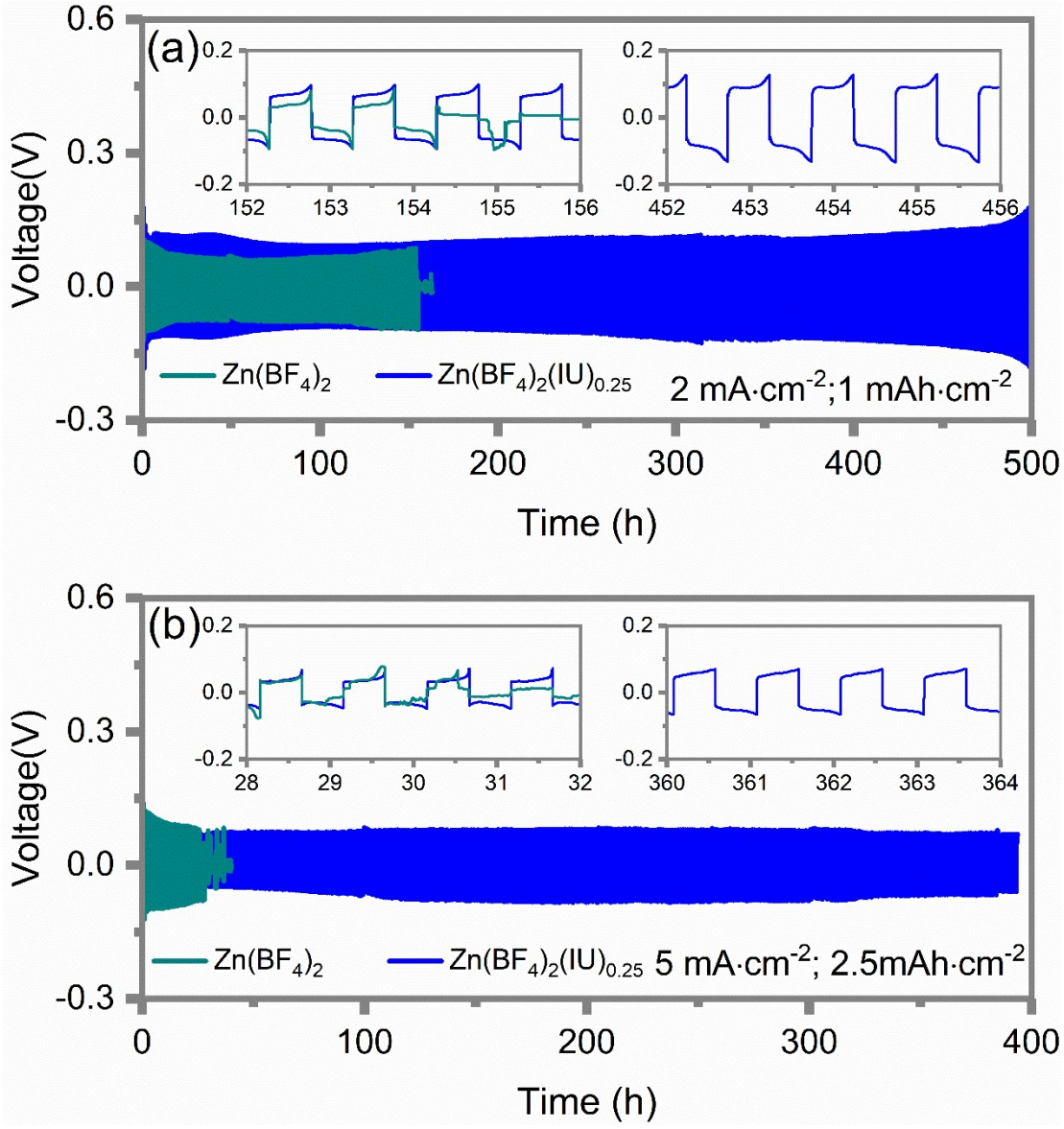

Figure S18. The charge/discharge curves of Zn||Zn symmetric cells (a) at current density of 2 mA·cm^{-2} with 1 mAh·cm^{-2} Zn cycled and (b) at current density of 5 mA·cm^{-2} with 2.5 mAh·cm^{-2} Zn cycled using $Zn(BF_4)_2$ and $Zn(BF_4)_2(IU)_{0.25}$ electrolytes.

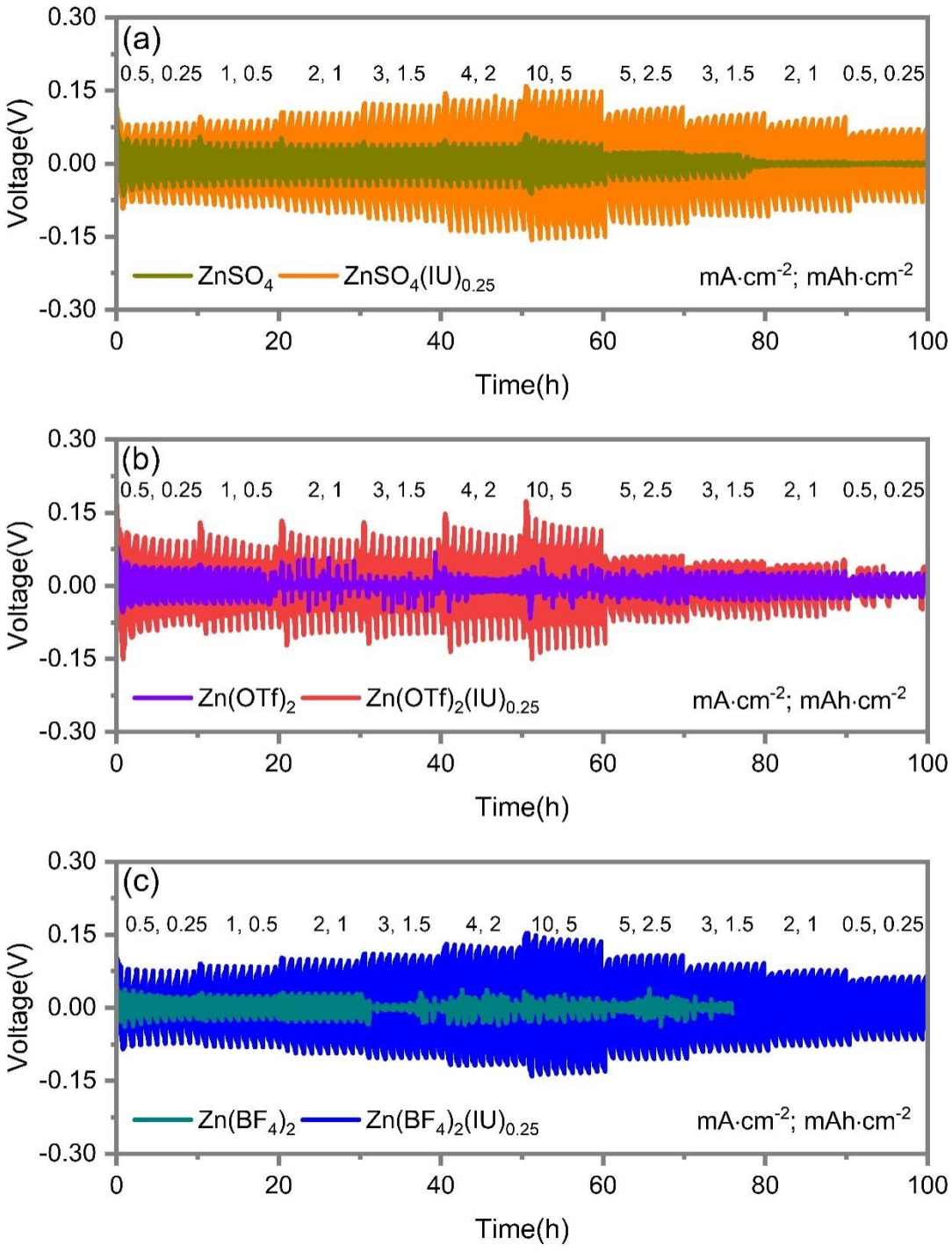

Figure S19. Rate capability of Zn||Zn symmetric cells using (a) $ZnSO_4$, $ZnSO_4(IU)_{0.25}$, (b) $Zn(OTf)_2$, $Zn(OTf)_2(IU)_{0.25}$ and (c) $Zn(BF_4)_2$, $Zn(BF_4)_2(IU)_{0.25}$ electrolytes.

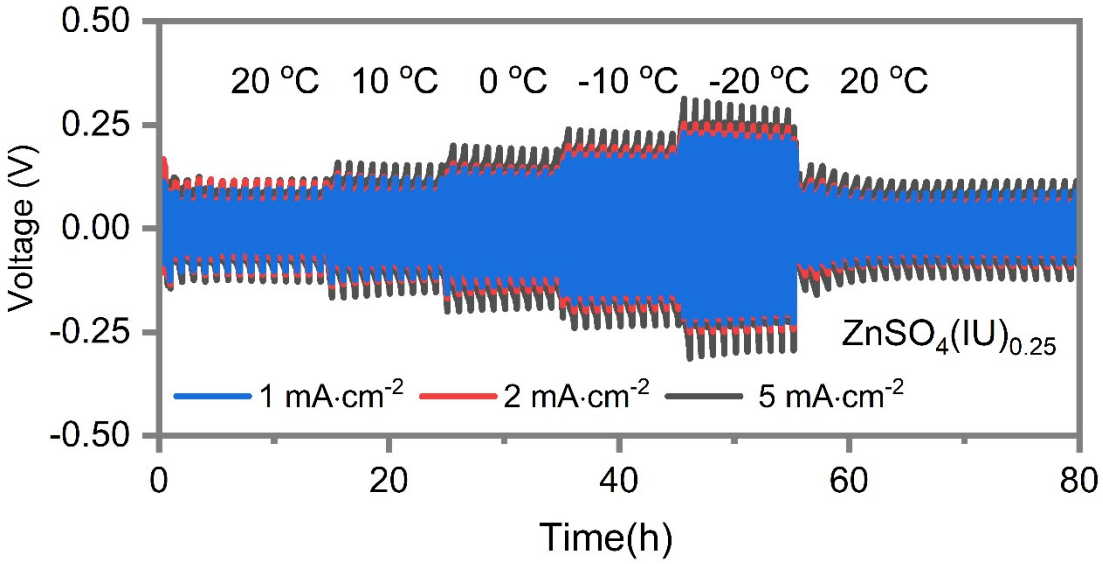

Figure S20. The charge/discharge curves of Zn||Zn symmetric cells at different temperature and different current density, respectively, using $ZnSO_4$ and $ZnSO_4(IU)_{0.25}$ electrolyte.

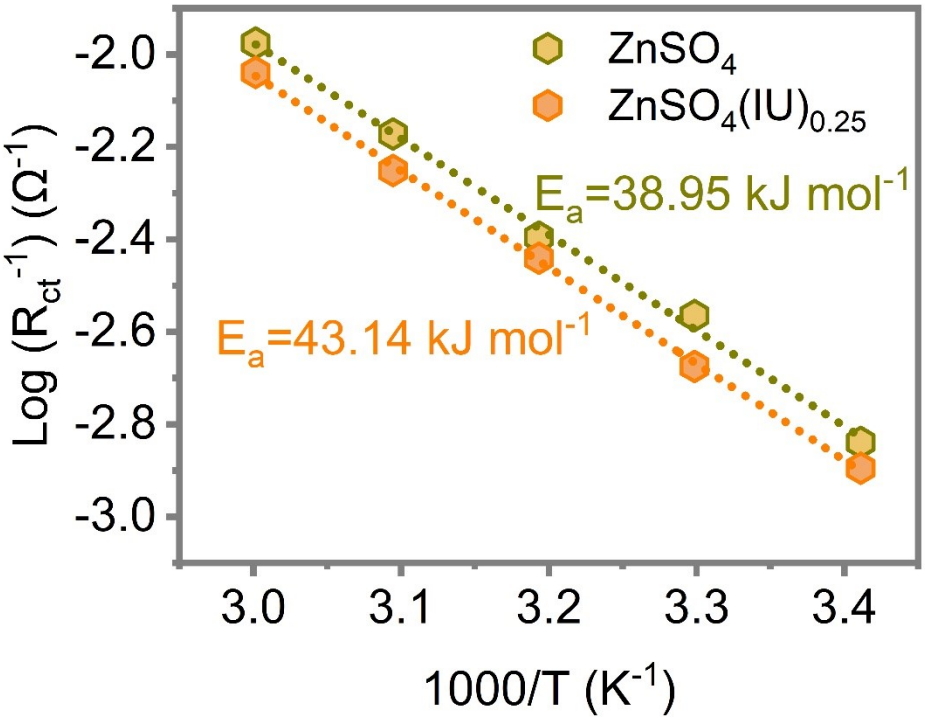

Figure S21. The calculated activation energies of Zn^{2+} diffusion in Zn/electrolyte interface by the Arrhenius equation.

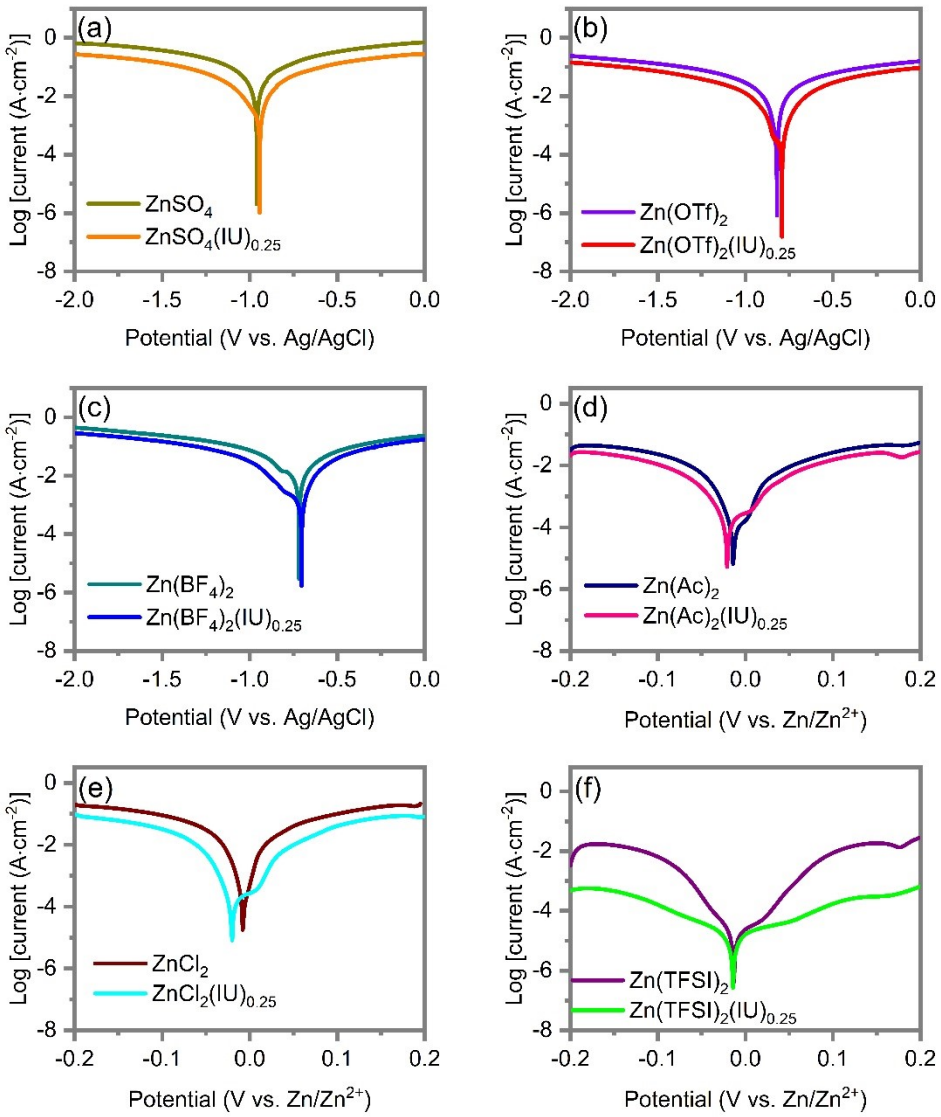

Figure S22. Linear polarization curves showing the corrosion on Zn metal using (a) $ZnSO_4$, $ZnSO_4(IU)_{0.25}$, (b) $Zn(OTf)_2$, $Zn(OTf)_2(IU)_{0.25}$, (c) $Zn(BF_4)_2$, $Zn(BF_4)_2(IU)_{0.25}$, (d) $Zn(Ac)_2$, $Zn(Ac)_2(IU)_{0.25}$, (e) $ZnCl_2$, $ZnCl_2(IU)_{0.25}$ and (f) $Zn(TFSI)_2$, $Zn(TFSI)_2(IU)_{0.25}$ electrolytes.

Table S3. Corrosion potential and corrosion current density at Zn anodes in several different electrolytes.

	Corrosion potential (V vs. Ag/AgCl)	Corrosion current density ($mA \cdot cm^{-2}$)
2 M $ZnSO_4$	-0.99	15.04
2 M $ZnSO_4(IU)_{0.25}$	-0.98	3.71
2 M $Zn(OTf)_2$	-0.83	26.03
2 M $Zn(OTf)_2(IU)_{0.25}$	-0.80	8.62
2 M $Zn(BF_4)_2$	-0.73	12.01
2 M $Zn(BF_4)_2(IU)_{0.25}$	-0.71	5.02

	Corrosion potential (V vs. Zn/Zn^{2+})	Corrosion current density ($mA \cdot cm^{-2}$)
2 M $Zn(Ac)_2$	-0.007	9.268
2 M $Zn(Ac)_2(IU)_{0.25}$	-0.024	4.543
2 M $ZnCl_2$	-0.001	36.141
2 M $ZnCl_2(IU)_{0.25}$	-0.004	10.018
2 M $Zn(TFSI)_2$	-0.012	1.792
2 M $Zn(TFSI)_2(IU)_{0.25}$	-0.018	0.026

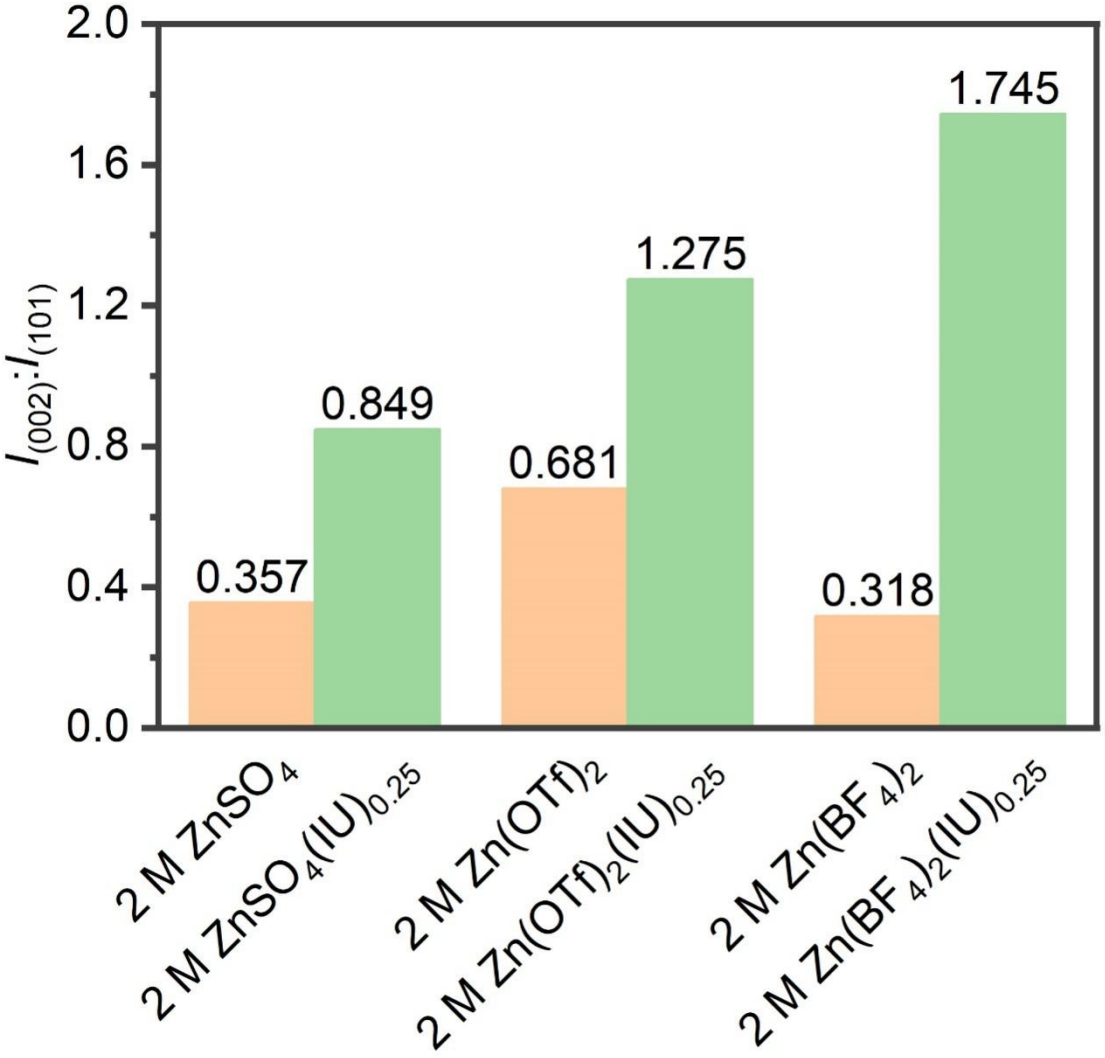

Figure S23. Ratio of XRD surface intensity of deposited zinc.

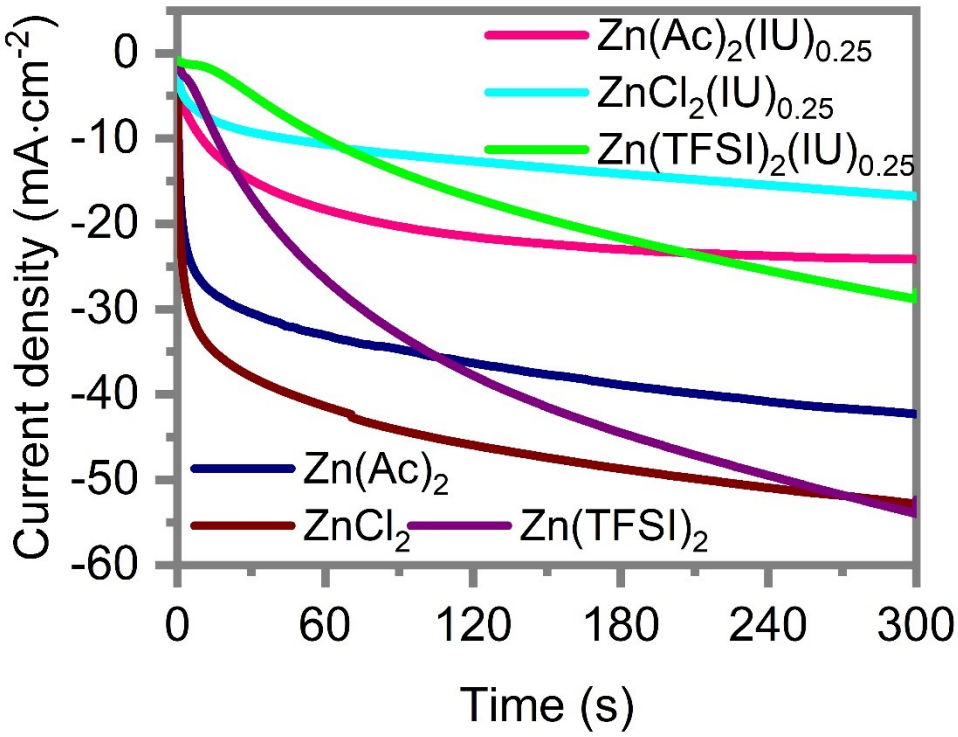

Figure S24. Chronoamperograms (CAs) of Zn metal using $Zn(Ac)_2$, $Zn(Ac)_2(IU)_{0.25}$, $ZnCl_2$, $ZnCl_2(IU)_{0.25}$, $Zn(TFSI)_2$ and $Zn(TFSI)_2(IU)_{0.25}$ electrolytes at a -150 mV overpotential.

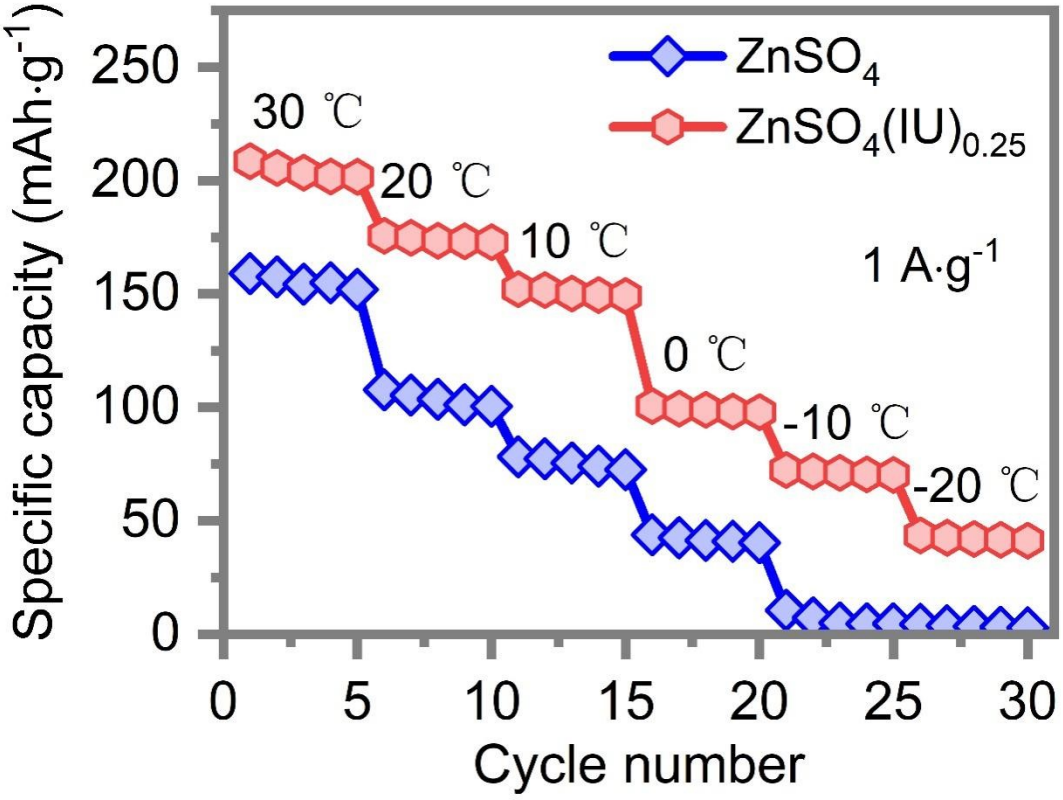

Figure S25. The performance of Zn||Br_2 full cells with 2 m $ZnSO_4$ and 2 m $ZnSO_4(IU)_{0.25}$ electrolytes at different temperature.

References

1. Kresse, G.; Furthmüller, J., Efficient iterative schemes for ab initio total-energy calculations using a plane-wave basis set. *Phys. Rev. B* **1996,** *54* (16), 11169.
2. Kresse, G.; Joubert, D., From ultrasoft pseudopotentials to the projector augmented-wave method. *Phys. Rev. B* **1999,** *59* (3), 1758.
3. Perdew, J. P.; Burke, K.; Ernzerhof, M., Generalized gradient approximation made simple. *Phys. Rev. Lett.* **1996,** *77* (18), 3865.
4. Grimme, S.; Antony, J.; Ehrlich, S.; Krieg, H., A consistent and accurate ab initio parametrization of density functional dispersion correction (DFT-D) for the 94 elements H-Pu. *J. Chem. Phys.* **2010,** *132* (15), 154104.
5. Neese, F., The ORCA program system. *Wiley Interdiscip. Rev.: Comput. Mol. Sci.* **2012,** *2* (1), 73-78.
6. Grimme, S.; Ehrlich, S.; Goerigk, L., Effect of the damping function in dispersion corrected density functional theory. *J. Comput. Chem.* **2011,** *32* (7), 1456-1465.
7. Krishnan, R.; Binkley, J. S.; Seeger, R.; Pople, J. A., Self-consistent molecular orbital methods. XX. A basis set for correlated wave functions. *J. Chem. Phys.* **1980,** *72* (1), 650-654.
8. Weigend, F.; Ahlrichs, R., Balanced basis sets of split valence, triple zeta valence and quadruple zeta valence quality for H to Rn: Design and assessment of accuracy. *Phys. Chem. Chem. Phys.* **2005,** *7* (18), 3297-3305.

9. Zhao, Y.; Truhlar, D. G., The M06 suite of density functionals for main group thermochemistry, thermochemical kinetics, noncovalent interactions, excited states, and transition elements: two new functionals and systematic testing of four M06-class functionals and 12 other functionals. *Theor. Chem. Acc.* **2008,** *120* (1), 215-241.

10. Hehre, W. J.; Ditchfield, R.; Pople, J. A., Self-consistent molecular orbital methods. XII. Further extensions of Gaussian-type basis sets for use in molecular orbital studies of organic molecules. *J. Chem. Phys.* **1972,** *56* (5), 2257-2261.

11. Rassolov, V. A.; Pople, J. A.; Ratner, M. A.; Windus, T. L., 6-31G* basis set for atoms K through Zn. *J. Chem. Phys.* **1998,** *109* (4), 1223-1229.

12. Marenich, A. V.; Cramer, C. J.; Truhlar, D. G., Universal solvation model based on solute electron density and on a continuum model of the solvent defined by the bulk dielectric constant and atomic surface tensions. *J. Phys. Chem. B* **2009,** *113* (18), 6378-6396.

13. Plimpton, S., Fast parallel algorithms for short-range molecular dynamics. *J. Comput. Phys.* **1995,** *117* (1), 1-19.

14. Wang, J.; Wolf, R. M.; Caldwell, J. W.; Kollman, P. A.; Case, D. A., Development and testing of a general amber force field. *J. Comput. Chem.* **2004,** *25* (9), 1157-1174.

15. Price, D. J.; Brooks, C. L., 3rd, A modified TIP3P water potential for simulation with Ewald summation. *J. Chem. Phys.* **2004,** *121* (20), 10096-103.

16. Jang, Y. H.; Chang, X. Y.; Blanco, M.; Hwang, S.; Tang, Y.; Shuler, P.; Goddard, W. A., The MSXX force field for the barium sulfate-water interface. *J. Phys. Chem. B* **2002,** *106* (38), 9951-9966.

17. Canongia Lopes, J. N.; Pádua, A. A., Molecular force field for ionic liquids III: Imidazolium, pyridinium, and phosphonium cations; chloride, bromide, and dicyanamide anions. *J. Phys. Chem. B* **2006,** *110* (39), 19586-19592.

18. Canongia Lopes, J. N.; Pádua, A. A., Molecular force field for ionic liquids composed of triflate or bistriflylimide anions. *J. Phys. Chem. B* **2004,** *108* (43), 16893-16898.

19. Doherty, B.; Zhong, X.; Gathiaka, S.; Li, B.; Acevedo, O., Revisiting OPLS Force Field Parameters for Ionic Liquid Simulations. *J. Chem. Theory Comput.* **2017,** *13* (12), 6131-6145.

20. Martinez, L.; Andrade, R.; Birgin, E. G.; Martinez, J. M., PACKMOL: a package for building initial configurations for molecular dynamics simulations. *J. Comput. Chem.* **2009,** *30* (13), 2157-2164.

21. Jewett, A. I.; Stelter, D.; Lambert, J.; Saladi, S. M.; Roscioni, O. M.; Ricci, M.; Autin, L.; Maritan, M.; Bashusqeh, S. M.; Keyes, T.; Dame, R. T.; Shea, J. E.; Jensen, G. J.; Goodsell, D. S., Moltemplate: A Tool for Coarse-Grained Modeling of Complex Biological Matter and Soft Condensed Matter Physics. *J. Mol. Biol.* **2021,** *433* (11), 166841.

22. Nosé, S., A unified formulation of the constant temperature molecular dynamics methods. *J. Chem. Phys.* **1984,** *81* (1), 511-519.

23. Hoover, W. G., Canonical dynamics: Equilibrium phase-space distributions. *Phys. Rev. A* **1985,** *31* (3), 1695-1697.

24. Berendsen, H. J.; Postma, J. v.; Van Gunsteren, W. F.; DiNola, A.; Haak, J. R., Molecular dynamics with coupling to an external bath. *J. Chem. Phys.* **1984,** *81* (8), 3684-3690.

25. Momma, K.; Izumi, F., VESTA 3 for three-dimensional visualization of crystal, volumetric and morphology data. *J. Appl. Crystallogr.* **2011,** *44* (6), 1272-1276.

26. Humphrey, W.; Dalke, A.; Schulten, K., VMD: visual molecular dynamics. *J. Mol. Graphics* **1996,** *14* (1), 33-38.